nature materials

Article

https://doi.org/10.1038/s41563-026-02533-6

Grain boundary stabilization of fluorite ferroelectrics

Received: 5 November 2025

Accepted: 5 February 2026

Shiyu Wang[1,2,6], Hai Zhong[1,3,6], Siyi Song[4,6], Ang Gao[4], Qinghua Zhang[1] ✉, Dong Su[1], Kuijuan Jin[1,2], Chen Ge[1,2] ✉ & Lin Gu[5] ✉

Grain boundaries (GBs) can tailor the macroscopic properties of polycrystalline materials via their intrinsic structural and electronic states. However, as independent heterointerfaces, their role in stabilizing grain phases remains largely unexplored, especially at the atomic scale. Here we report that chemically ordered heterogeneous GBs in ZrO_2 thin films act as active stabilizers of a metastable polar phase. The atomically sharp and ordered La(Sr)–Mn–O configurations at GBs are identified at the atomic scale. The resultant charge ordering and bond covalency of the GBs are validated by four-dimensional scanning transmission electron microscopy. This structural motif induces e_g/t_{2g} orbital ordering of Mn ions at GBs, modulating Zr–O bond strength to stabilize the polar phase. This work establishes a GB-centric paradigm for engineering nanoscale phase diagrams, offering a promising strategy for designing metastable functional materials via GB chemistry.

Grain boundaries (GBs), ubiquitous topological defects in polycrystalline materials, critically govern the macroscopic properties of many technological materials, including mechanical strength, radiation tolerance and thermal conductivity[1–6]. For example, dense GB networks impede dislocation motion, yielding pronounced strengthening and hardening in nanostructured metals and superhard materials[7–9]. Graphene-decorated GBs suppress grain coarsening for low lattice thermal conductivity while preserving the high electronic performance of thermoelectrics[10–12]. Despite these advances, prior strategies focusing on segregation, defect engineering or microstructural modification have consistently regarded GBs merely as auxiliary units for property regulation[13–15]. Yet, as dominant and high-volume-fraction planar defects in nanograins, GBs possess inherently distinct and independent structural and electronic degrees of freedom[16–18], which may modify atomic diffusion pathways and local electronic states along the GB. These features suggest that GBs are not only auxiliary regulators[19–21], but also act as independent heterointerfaces capable of directly stabilizing grain phase structures and inducing emergent functionalities. However, the GB-mediated phase regulation, which would unlock a new paradigm of GBs in phase control and functional innovation, remains essentially unexplored.

The possibility of GB-mediated phase control has become increasingly notable, especially with the discovery of ferroelectricity in nanocrystalline fluorites such as HfO_2- and ZrO_2-based films[22–28]. The ferroelectricity stems from a metastable non-centrosymmetric orthorhombic (O) phase, whose intrinsic instability induces severe wake-up and fatigue effects[29–35]. While factors such as strain[36–38], doping[39–43], oxygen vacancies[42] and surface energy[32,43] have been proposed to explain the O-phase stabilization, their roles are either context dependent or lack atomic-level validation. For instance, stable ferroelectricity in free-standing HfO_2/ZrO_2 thin films confirms that substrate-induced strain is not the intrinsic driver for sustaining the polar phase[44,45]. Yet, these ultrathin films are inherently nanocrystalline with a high density of GBs, which should contribute substantially to the energy landscape of ferroelectric phases. However, the role of GBs in stabilizing the O phase at the nanoscale has rarely been mentioned,

---

[1]Beijing National Laboratory for Condensed Matter Physics, Institute of Physics, Chinese Academy of Sciences, Beijing, China. [2]School of Physical Sciences, University of Chinese Academy of Sciences, Beijing, China. [3]School of Physics and Optoelectronic Engineering, Ludong University, Yantai, China. [4]Institute of Environmental and Applied Chemistry, College of Chemistry, Central China Normal University, Wuhan, China. [5]Beijing National Center for Electron Microscopy and Laboratory of Advanced Materials, Department of Materials Science and Engineering, Tsinghua University, Beijing, China. [6]These authors contributed equally: Shiyu Wang, Hai Zhong, Siyi Song. ✉e-mail: zqh@iphy.ac.cn; gechen@iphy.ac.cn; lingu@tsinghua.edu.cn

mainly due to the prevailing perception of GBs as auxiliary units, complex phase coexistence and difficulties in precisely resolving the atomic-scale structure and chemical composition of GBs[43,46].

Here, we report that a chemically ordered La(Sr)–Mn–O superstructure at GBs stabilizes the metastable ferroelectric O phase in ZrO_2 thin films. The atomically sharp and ordered La(Sr)–Mn–O configurations, exclusively pinned at GBs, are identified by atomic-scale imaging and electron energy loss spectroscopy (EELS). The resultant charge ordering and distinct Mn–O electronic interactions are comprehensively validated by four-dimensional scanning transmission electron microscopy (4D-STEM). With the aid of first-principles calculations, we reveal an ordered e_g/t_{2g} orbital arrangement of Mn^{3+}/Mn^{4+} at GBs. Such orbital ordering periodically modulates Zr–O bond strength via reduced orbital overlap, ultimately stabilizing the ferroelectric state. These findings establish a stabilization mechanism for metastable polar phases via a new GB chemistry, opening avenues for ultrastable nanoelectronics.

Heterogeneous GBs in ferroelectric ZrO_2 thin films

To investigate the stabilization mechanism of the metastable ferroelectric phase in ZrO_2, we prepared polycrystalline ZrO_2 thin films with abundant GBs via pulsed-laser deposition (PLD), grown on single-crystal $SrTiO_3$ substrates with a $La_{0.67}Sr_{0.33}MnO_3$ (LSMO) buffer layer. Notably, ZrO_2 exhibits three prominent polymorphs, tetragonal (T), monoclinic (M) and orthorhombic (O), with nearly identical formation energies; among these, the polar O phase is the most metastable and difficult to stabilize, as schematically illustrated in Fig. 1a (refs. 35,44,45). Our experiments confirmed the LSMO buffer layer is indispensable for O-phase formation[47–49]: X-ray diffraction confirmed the high crystalline quality of O phase in these buffered films, while ZrO_2 films on $LaMnO_3$ (LMO) or $SrMnO_3$ (SMO) buffers lacked the O phase and were dominated by non-polar T/M phases. Complementary polarization–electric field (*P*–*E*) and current–electric field (*I*–*E*) hysteresis measurements further validated ferroelectric behaviour in LSMO-buffered films, whereas LMO/SMO-buffered films exhibited no detectable ferroelectric loops (Extended Data Fig. 1).

To uncover the microstructural origin of LSMO-enabled O-phase stabilization, we characterized the GB network and elemental distribution of LSMO-buffered ZrO_2 films using high-angle annular dark field (HAADF) imaging and EELS mapping. Large field-of-view HAADF images revealed pervasive ordered GBs throughout the predominantly O-phase ZrO_2 films, which consist of nanocrystals with grain sizes of several nanometres (Fig. 1b–d and Extended Data Fig. 2). Unexpectedly, EELS elemental mapping revealed selective segregation of La, Sr and Mn at these GBs, with these species absent in grain interiors (Fig. 1e–g and Extended Data Fig. 3). Given the use of LSMO buffer layers during the PLD process, we deduce that La/Sr/Mn elements diffused from the buffer layer into the GBs of ZrO_2 matrix, forming a stable and homogeneous GB structure that remains intact even after free-standing sample preparation and imaging (Extended Data Figs. 4 and 5). Notably, previous studies overlooked the potential elemental segregation at GBs from the LSMO buffer layer, due to the challenge of detecting atomically sharp heterogeneous layers between nanograins. Here, we resolved this by combining a K3 direct detection counting detector (GIF Continuum K3) with high signal-to-noise ratio and free-standing sample geometry, enabling single-atom-column chemical identification. This advance laid the groundwork for subsequent atomic-scale structural determination of GBs.

Atomic structure of the distinct La(Sr)–Mn–O segregated GBs

Given the selective segregation of La/Sr/Mn at GBs, we determined the atomic structure of these GBs via integrated differential phase contrast (iDPC) imaging, a technique with inherent high sensitivity to

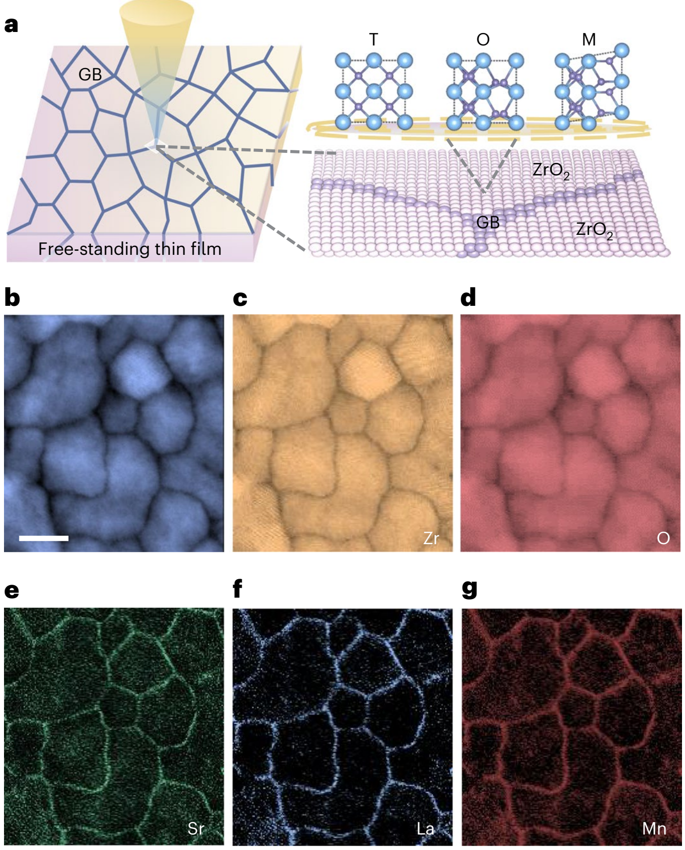

Fig. 1 | La/Sr/Mn segregated GBs in ZrO_2 thin films. a, Schematic of the polymorphic characteristics of free-standing ZrO_2 thin films, where abundant GBs are critical for phase stability. The upper-right inset shows atomic models of the three predominant phases (tetragonal T, monoclinic M, orthorhombic O); the polar O phase is metastable and difficult to stabilize. **b**, HAADF image of textured ZrO_2 nanocrystals with prominent GBs marked by dark contrast regions. **c**–**g**, Corresponding EELS elemental mappings of Zr (**c**), O (**d**), Sr (**e**), La (**f**) and Mn (**g**) from the region in **b**. Scale bar, 10 nm. Sr, La and Mn are selectively enriched along GBs, whereas Zr is depleted at these boundaries.

light elements such as oxygen. As shown in Fig. 2a, the GB exhibits an atomically sharp, highly ordered and periodic configuration. By correlating contrast intensity with structural simulations and subsequent elemental mapping (Supplementary Fig. 1), we assigned atomic species: green and blue spheres denote Mn and Zr atoms, respectively, while red spheres represent La/Sr-mixed atom columns. For clarity, we overlaid atomic positions on the same iDPC image using representative spheres and circles (Fig. 2b). Notably, Mn atoms occupy two crystallographically distinct sites (labelled Mn_1 and Mn_2) with differing coordination numbers, arranged in a periodic sequence along the GB.

To quantify these structural features, we further extracted the GB motif and measured tilt angles and neighbouring atomic distances (Fig. 2c). The measured tilt angles, 47.6° and 57.2°, represent a distinct departure from the 53° angle of the standard $\Sigma5[210]$ ZrO_2 GB in the T-phase[50], confirming that La(Sr)–Mn–O segregation induces structural modification of GBs. Analysis of Mn coordination environments (Fig. 2d) reveals clear differentiation between Mn_1 and Mn_2: Mn_1 adopts 6-fold coordination at the apexes of two trigonal pyramids, while Mn_2 is 5-fold coordinated at the centre of a tetragonal pyramid. Moreover, projected Mn_1–O bond lengths (1.14, 1.55 and 0.75 Å) are shorter than those of Mn_2–O bonds (1.41, 1.68 and 0.83 Å), indicating stronger electronic interactions. Thus, the ordered GB structure comprises repeating units with two submotifs, featuring different tilt angles, atomic distances and resultant distinct Mn coordination environments.

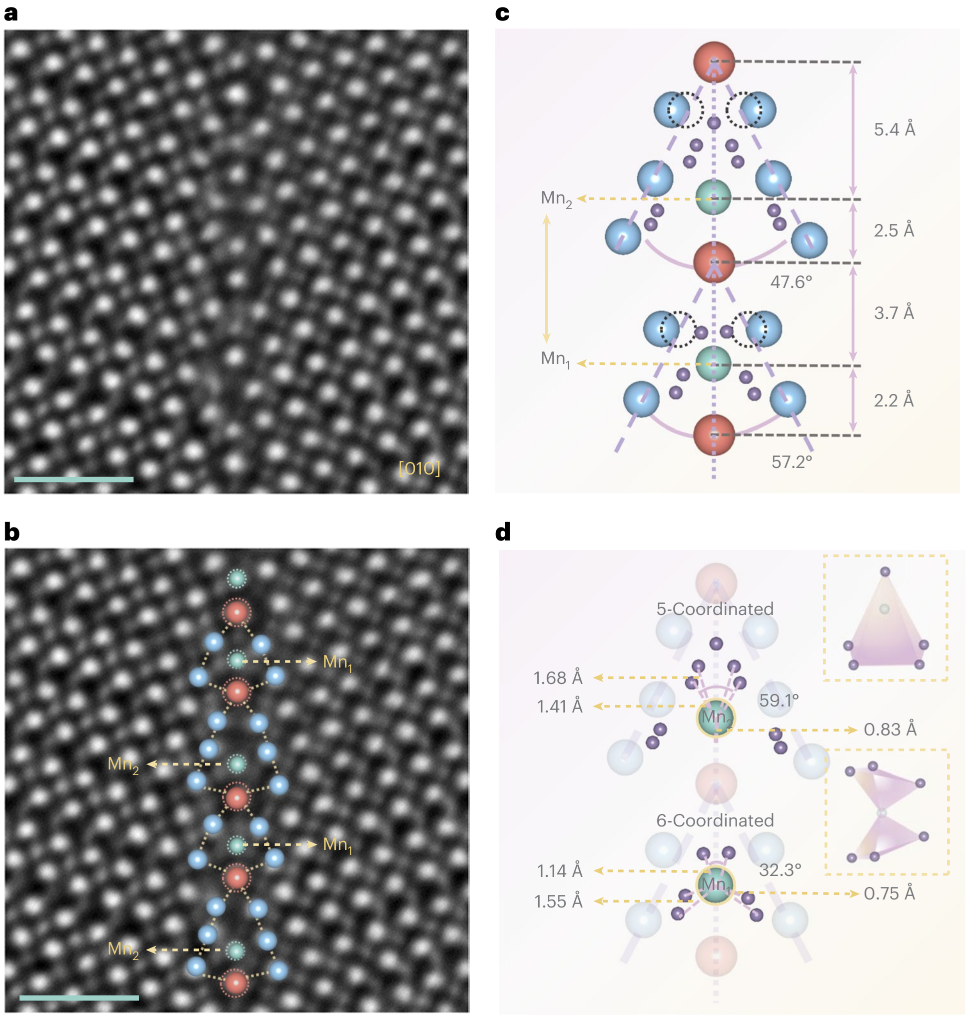

Fig. 2 | Atomic structure and Mn coordination at GBs. a, Atomic-resolution iDPC image of the La(Sr)–Mn–O segregated GB phase viewed along the [010] zone axis in ferroelectric O-phase ZrO_2. Scale bar, 1 nm. **b**, The same iDPC image overlaid with atomic models and circles for clear visualization of atomic positions. **c**, Schematic of the GB structural unit, showing key tilt angles and projected atomic distances derived from experimental data. The black dashed circles mark the original lattice sites of Zr atoms in the ideal ZrO_2 lattice, which deviate from their intrinsic positions due to lattice distortion induced by the La(Sr)–Mn–O segregated GB. **d**, Schematic of Mn_1 (6-fold coordination) and Mn_2 (5-fold coordination) ions, marking Mn–O bond lengths and bond angles derived from experimental data.

Valence state of Mn ions and strain configuration at GB

To verify elemental occupation and electronic structure at La(Sr)–Mn–O segregated GBs, we performed atomic-resolution EELS mapping using a direct electron detector, which enables high noise resistance under low signal levels. Zr atoms show a marked depletion at the GB relative to the bulk lattice, whereas La, Sr and Mn atoms are enriched at the GB with minimal diffusion into the surrounding ZrO_2 bulk regions (Fig. 3a). Specifically, the brightest spots highlighted by dotted pink squares along the GB reveal co-occupancy of La and Sr at the same lattice sites, with Mn atoms residing at adjacent sites. The alternating L_3-edge peaks at 645.63 and 644.45 eV in the EELS spectra (Fig. 3b) further confirm two types of Mn ion, arranged periodically along the GB with different Mn–O electronic interactions. Corresponding L_3/L_2 ratio profiles (Fig. 3c) indicate cation valence states, with reference ratios marked as blue-shaded bands[51], showing obvious alternating Mn^{4+}/Mn^{3+} along the GB, implying varied orbital overlap with adjacent oxygen ions, which should be critical for stabilizing the O phase.

Besides charge ordering of Mn ions, segregated La/Sr/Mn ions also introduce local lattice distortions at GBs. Bulk ZrO_2 exhibits near-zero distortion while GB regions show marked deviations, reflecting localized strain induced by these segregated elements (Fig. 3d), as supported by strain component maps (ε_y, Fig. 3e; ε_x, Supplementary Fig. 2), which quantify atomic displacements of all cations (Zr, Mn, La/Sr) relative to the ideal O-phase ZrO_2 lattice and thus directly map the spatial distribution of lattice strain. Specifically, the La/Sr ions generate tensile strain by shifting towards the upper-right corner of the La/Sr-3Zr quadrilateral, whereas the Mn ions produce compressive strain by moving towards the lower-left corner of the Mn-3Zr quadrilateral, with Mn_1 showing weaker strain and Mn_2 stronger strain. We further quantified polarization near the GB region based on oxygen off-centre displacement in each unit cell (Fig. 3f). The ZrO_2 grain exhibits typical ferroelectric behaviour with alternating polar and non-polar layers, while the GB shows a periodically varying polarization state driven by La/Sr/Mn segregation and oxygen ion displacement. In summary, the La(Sr)–Mn–O segregated GB is characterized by La/Sr–Mn ordering with alternating Mn^{4+}/Mn^{3+} valence states, which accommodate periodic strain patterns and polarization discontinuity at this coherent GB.

Orbital ordering and GB stabilization mechanism

To clarify the nature of electronic interactions at the La(Sr)–Mn–O segregated GB, we performed real-space charge density measurements

https://doi.org/10.1038/s41563-026-02533-6

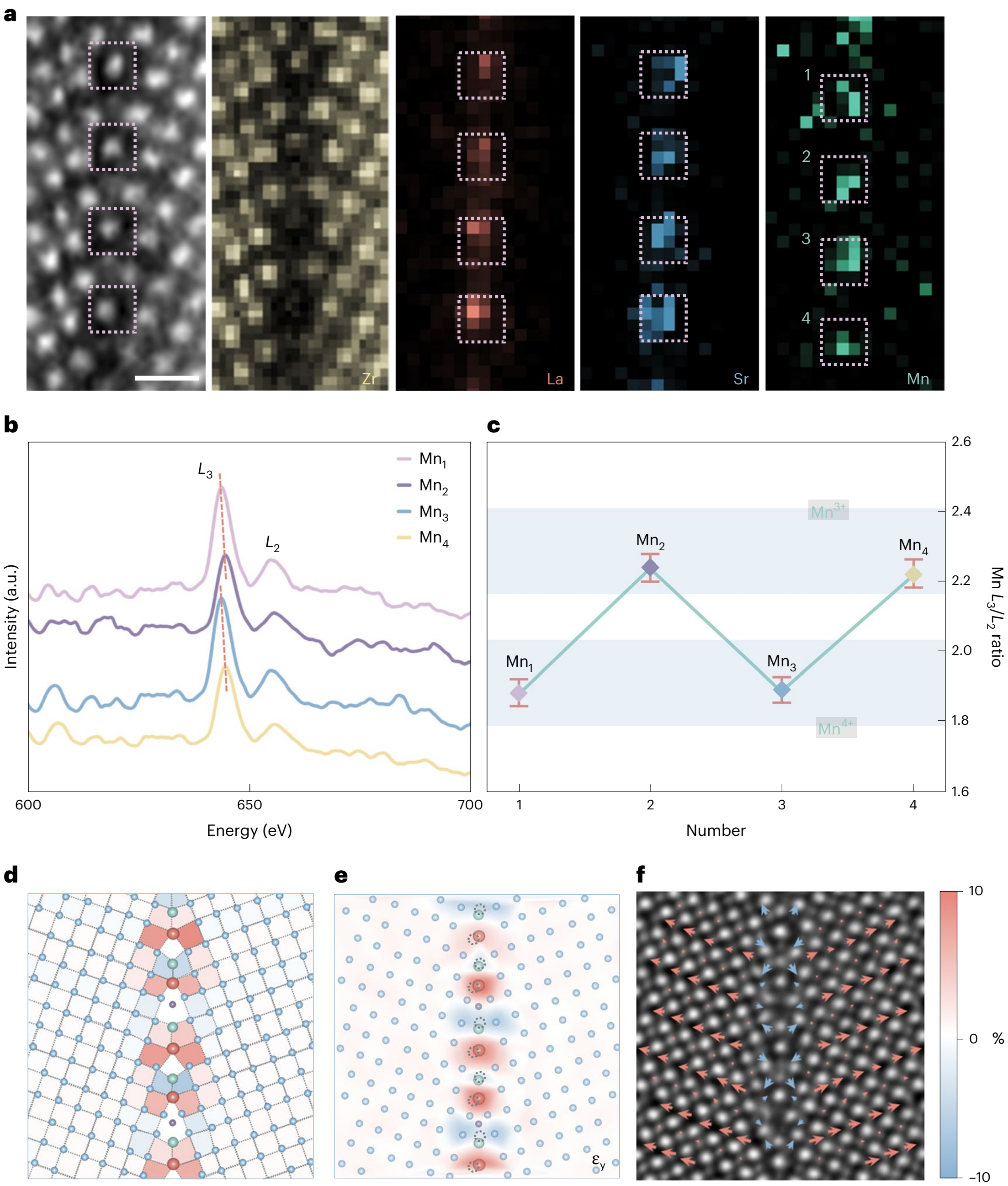

Fig. 3 | Atomic-resolved elemental mapping, Mn valence state, strain and polarization of the GB phase. a, HAADF-STEM image and atomic-resolution EELS mapping of the La(Sr)–Mn–O segregated GB along the [010] zone axis, showing the distribution of Zr (yellow), La (red), Sr (blue) and Mn (green) along the GB, especially the preferential enrichment of La/Sr/Mn ions and depletion of Zr. Dashed pink squares highlight periodic lattice sites with La/Sr co-occupancy and adjacent Mn-occupied sites. Scale bar, 1 nm. **b**, Mn *L*-edge profiles from four Mn ions labelled 1–4 in **a**, exhibiting two distinct electronic structures in ordered arrangement. **c**, Mn L_3/L_2 ratio profile, where 1–4 correspond to four Mn ions labelled in **a**, with blue-shaded bands indicating reference ranges for Mn^{3+} and Mn^{4+}. The error bars represent the standard deviation of the mean values, derived from the errors introduced in background subtraction baseline variations and data fluctuation among spectra. **d**, Lattice distortion mapping relative to bulk ZrO_2. **e**, Unit-cell-scale ε_y strain mapping, corresponding to strain parallel to the GB. Grey circles mark the original atomic sites in the ideal ZrO_2 lattice. The rightmost colour bar applies to **d** and **e**, representing the percentage of relative lattice distortion and strain. **f**, Polarization mapping near the GB, where red and blue arrows represent polarization states in the bulk ZrO_2 and GB, respectively.

via 4D-STEM. Charge density maps reveal ordered La(Sr)–Mn–O motifs along the GB, with each atom surrounded by distinct negative charge pockets (Fig. 4a), indicating shared electron density and, thus, enhanced covalency in the Mn–O bonding. After subtracting the nuclear charge contribution from the total charge density, we clearly identified two types of Mn ion with distinct charge densities, as highlighted by yellow lines. By contrast, negative charge pockets between O and Zr columns diminish near the GB relative to the bulk, corresponding to reduced Zr–O covalency.

To link these experimental charge observations to orbital-level mechanisms, we analysed charge density difference via first-principles calculations. Direct visualization shows substantial charge transfer from Zr–O to Mn–O bonds at the GB: electron density accumulates prominently around Mn–O bond regions, while electron depletion occurs in Zr–O domains adjacent to the GB (Fig. 4b and Supplementary Fig. 3). The partial density of states (PDOS) clarifies that Mn_1 interacts predominantly via e_g orbitals, while Mn_2 interacts primarily through t_{2g} orbitals. This gives rise to alternating Mn_1-e_g and

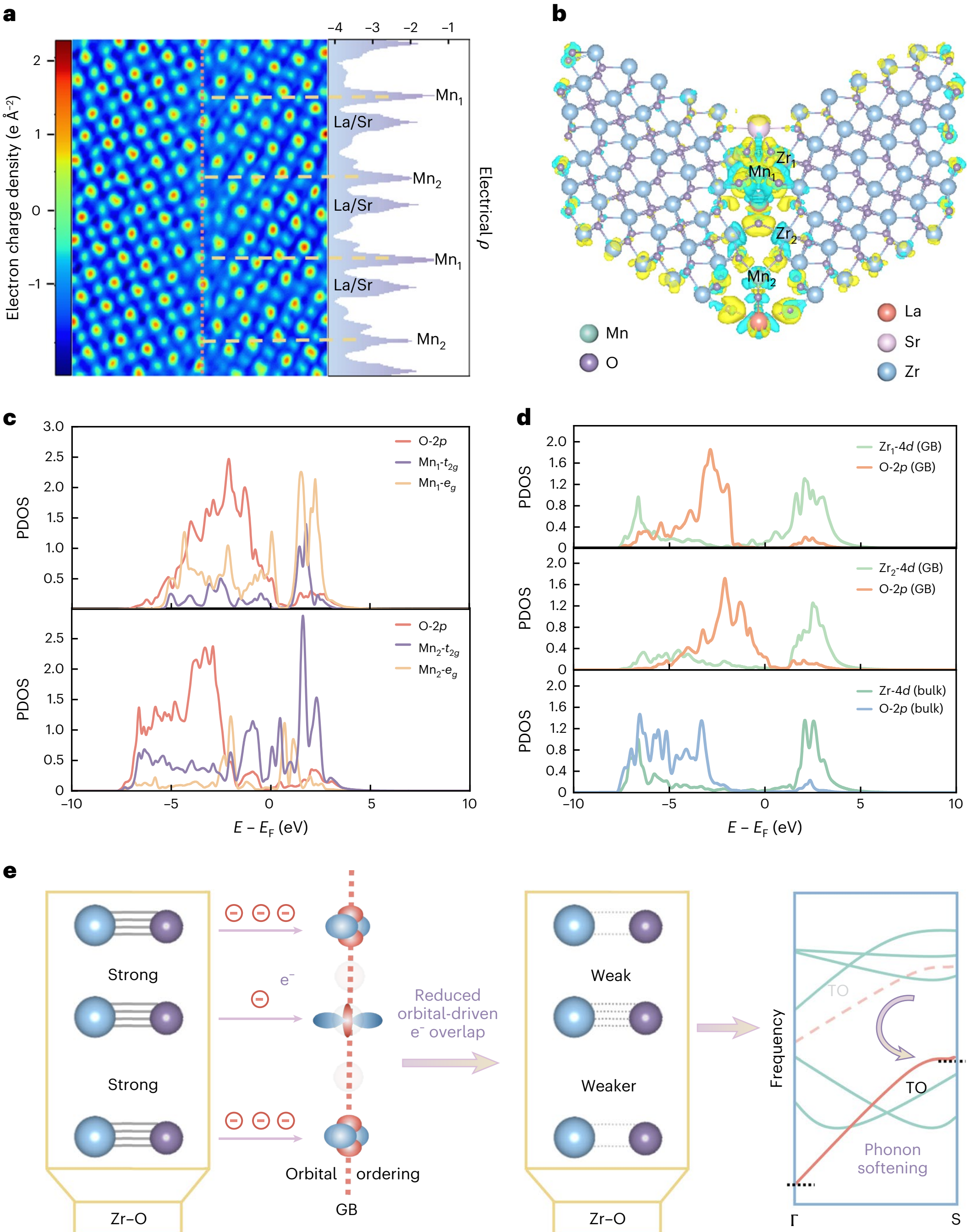

Fig. 4 | Charge and orbital ordering analysis and ferroelectric stabilization mechanism. a, Total charge density map reconstructed from 4D-STEM data acquired along the [010] zone axis, revealing periodically ordered La(Sr)–Mn–O motifs along the GB and distinct negative charge distributions around atoms. The orange vertical dashed line serves as a guideline to mark the position of the GB for clear visualization. Electron charge density profile along GB highlights alternating charge density values for two Mn ion types. **b**, Charge density difference map of ZrO_2 with the La(Sr)–Mn–O segregated GB. The blue regions denote electron depletion, and yellow regions indicate electron accumulation. **c**, PDOS analysis of orbital interactions between Mn_1/Mn_2 and neighbouring oxygen ions. **d**, PDOS of ZrO_2 near the GB and in the bulk, showing shifts in Zr 4d–O 2p peaks that reflect weakened Zr–O bonding at the GB. **e**, Schematic of the orbital ordering-modulated GB stabilization mechanism. The Zr–O bonds are weakened by alternating Mn e_g/t_{2g} orbitals via reduced orbital electron overlap, which softens the TO phonon mode and stabilizes the ferroelectric phase. Γ and S represent key momentum space positions for characterizing the softening of TO phonon modes in the fluorite ferroelectric lattice.

Mn_2-t_{2g} orbital ordering in the La(Sr)–Mn–O segregated GB structure. Moreover, Mn_1 e_g–O 2p bonding is stronger than Mn_2 t_{2g}–O 2p, as indicated by more intense and broader hybridization peaks between Mn_1 e_g and O 2p orbitals in the PDOS (Fig. 4c), indicating higher orbital overlap efficiency[52,53]. Consequently, Zr 4d–O 2p orbital overlap is systematically weakened near the GB, with Zr_1–O bonds exhibiting weaker strength than Zr_2–O bonds (Fig. 4d). Thus, the Mn_1-e_g and Mn_2-t_{2g} orbital ordering at the GB periodically modulates Zr–O bonding with periodic weakened interactions, which is crucial for the stabilization of the O phase[54–57]. This modulated bonding alters the phonon dispersion by softening the transverse optical (TO) phonon mode, which matches the lattice periodicity of the O phase[58–61], in turn stabilizing the metastable phase with alternating polar and non-polar sublayers (Fig. 4e).

Discussions

To verify the GB structure, we designed eight $La_{1-x}Sr_xMnO_3$ GB structural units by substituting Zr atoms with La/Sr ions and introducing interstitial Mn atoms (Supplementary Figs. 4 and 5), and we calculated the relative energy with respect to the pure ZrO_2 GB and plotted the energy difference between the O and M phases (Supplementary Fig. 6). Notably, the LSMO unit exhibits the lowest energy in the O phase and greater stability than its M-phase counterpart. The LSMO doping ratio also ensures periodic GB ordering and Mn^{4+}/Mn^{3+} valence alternation, with resulting orbital ordering that is crucial for phase stabilization, as verified in our experiments. In addition, in situ iDPC imaging confirms that La(Sr)–Mn–O segregated GB configurations ensure phase stability. ZrO_2 nanocrystals with chemically ordered GBs undergo approximately 800 cycles of T–O phase transitions within 8 min under electron irradiation, without degrading into the non-polar M phase (Supplementary Fig. 7). However, switching the buffer layer from LSMO to LMO/SMO reduces GB order and decreases the O-phase fraction, as shown in Supplementary Fig. 8. This directly demonstrates that GB energy dominates the total system energy, and our quantitative estimates further confirm that it accounts for a large proportion of the overall energy (Supplementary Note 1). This result complements previous studies on LSMO's role of stabilizing the O phase, including interfacial/mechanical reconstruction[62,63], domain matching epitaxy[48] and hole doping[49], by highlighting a previously overlooked factor, namely the critical contribution of high-density GBs in nanocrystals. Notably, the effectiveness of this GB-mediated stabilization mechanism is thickness dependent, governed by surface-GB energy competition, establishing 20 nm as the upper thickness limit for effective GB-stabilized ferroelectricity (Supplementary Fig. 9).

Moreover, since the discovery of ferroelectricity in Si-doped HfO_2 thin films, dopants have been intensely studied for stabilizing ferroelectric phases, typically via introducing oxygen vacancies to maintain charge neutrality and facilitate non-polar-to-polar transitions[64–66]. However, these studies focused primarily on dopant types and concentrations, overlooking atomic-scale distribution of dopants within nanocrystals, particularly at GBs. This oversight is critical, as impurity/dopant segregation to GBs is a prevalent phenomenon in polycrystalline materials. Meanwhile, fluorite oxides consist of nanograins, where high-density GBs exert a more substantial influence on surface energy than those in micrometre-sized grains at thickness below 10 nm. Notably, within this effective thickness range, these dopants, when segregated at GBs with ordered site occupancy as observed in our work, can modify local orbital interactions in a way that stabilizes the metastable ferroelectric phase.

In conclusion, our atomic-scale investigations reveal that chemically ordered GB configurations effectively stabilize the metastable ferroelectric phase in ZrO_2 thin films via elemental segregation from the buffer layers. The e_g–t_{2g} orbital ordering of the Mn^{3+}/Mn^{4+} along the GB induces alternating interactions with oxygen ions and periodically reduced Zr–O bonding strength, which softens the TO phonon and thus stabilizes the ferroelectric phase. These findings demonstrate the critical role of GBs in stabilizing ferroelectricity and establish a new paradigm for phase control through GB segregation engineering. This discovery solves a long-standing mechanism puzzle, provides a new dimension to nanoscale phase diagrams and opens new avenues for designing nanoscale metastable materials via GB chemistry.

Online content

Any methods, additional references, Nature Portfolio reporting summaries, source data, extended data, supplementary information, acknowledgements, peer review information; details of author contributions and competing interests; and statements of data and code availability are available at https://doi.org/10.1038/s41563-026-02533-6.

References

1. Tong, K. et al. Structural transition and migration of incoherent twin boundary in diamond. *Nature* **626**, 79–85 (2024).
2. Buban, J. et al. Grain boundary strengthening in alumina by rare earth impurities. *Science* **311**, 212–215 (2006).
3. Luo, J. et al. The role of a bilayer interfacial phase on liquid metal embrittlement. *Science* **333**, 1730–1733 (2011).
4. Wang, L. et al. Tracking the sliding of grain boundaries at the atomic scale. *Science* **375**, 1261–1265 (2022).
5. Zhang, B. B. et al. Inhibiting creep in nanograined alloys with stable grain boundary networks. *Science* **378**, 659–663 (2022).
6. Wei, J. et al. Direct imaging of atomistic grain boundary migration. *Nat. Mater.* **20**, 951–955 (2021).
7. Hu, J. et al. Grain boundary stability governs hardening and softening in extremely fine nanograined metals. *Science* **355**, 1292–1296 (2017).
8. Huang, Q. et al. Nanotwinned diamond with unprecedented hardness and stability. *Nature* **510**, 250–253 (2014).
9. Irifune, T. et al. Ultrahard polycrystalline diamond from graphite. *Nature* **421**, 599–600 (2003).
10. Lin, Y. et al. Thermoelectric power generation from lanthanum strontium titanium oxide at room temperature through the addition of graphene. *ACS Appl. Mater. Interfaces* **7**, 15898–15908 (2015).
11. Zong, P. et al. Skutterudite with graphene-modified grain-boundary complexion enhances *zT* enabling high-efficiency thermoelectric device. *Energy Environ. Sci.* **10**, 183–191 (2017).
12. Feng, X. et al. Graphene promoted oxygen vacancies in perovskite for enhanced thermoelectric properties. *Carbon* **112**, 169–176 (2017).
13. Zhang, Z. et al. Direct atom-resolved imaging of oxides and their grain boundaries. *Science* **302**, 846–849 (2003).
14. Huang, P. Y. et al. Grains and grain boundaries in single-layer graphene atomic patchwork quilts. *Nature* **469**, 389–392 (2011).
15. Li, X. Y. et al. Constrained minimal-interface structures in polycrystalline copper with extremely fine grains. *Science* **370**, 831–836 (2020).
16. Beaudry, D. C. et al. Exceptional hardness in multiprincipal element alloys via hierarchical oxygen heterogeneities. *Sci. Adv.* **10**, eado9697 (2024).
17. Li, X. Y., Zhou, X. & Lu, K. Rapid heating induced ultrahigh stability of nanograined copper. *Sci. Adv.* **6**, eaaz8003 (2024).
18. Barr, C. M. et al. The role of grain boundary character in solute segregation and thermal stability of nanocrystalline Pt–Au. *Nanoscale* **13**, 3552–3563 (2021).
19. Wang, Z. et al. Atom-resolved imaging of ordered defect superstructures at individual grain boundaries. *Nature* **479**, 380–383 (2011).
20. Chen, K. C. et al. Observation of atomic diffusion at twin-modified grain boundaries in copper. *Science* **321**, 1066–1069 (2008).
21. Zhou, X. et al. High-pressure strengthening in ultrafine-grained metals. *Nature* **579**, 67–72 (2020).
22. Luo, Q. et al. A highly CMOS compatible hafnia-based ferroelectric diode. *Nat. Commun.* **11**, 1391 (2020).
23. Boescke, T. S. et al. Ferroelectricity in hafnium oxide thin films. *Appl. Phys. Lett.* **99**, 102903 (2011).
24. Mueller, J. et al. Ferroelectricity in Simple Binary ZrO_2 and HfO_2. *Nano Lett.* **12**, 4318–4323 (2012).
25. Hoffmann, M. et al. Stabilizing the ferroelectric phase in doped hafnium oxide. *J. Appl. Phys.* **118**, 072006 (2015).
26. Cheema, S. S. et al. Ultrathin ferroic HfO_2-ZrO_2 superlattice gate stack for advanced transistors. *Nature* **604**, 65–71 (2022).
27. Schroeder, U. et al. The fundamentals and applications of ferroelectric HfO_2. *Nat. Rev. Mater.* **7**, 653–669 (2022).

28. Si, M. et al. A ferroelectric semiconductor field-effect transistor. *Nat. Electron.* **2**, 580–586 (2019).
29. Park, M. H. et al. Evolution of phases and ferroelectric properties of thin $Hf_{0.5}Zr_{0.5}O_2$ films according to the thickness and annealing temperature. *Appl. Phys. Lett.* **102**, 242905 (2013).
30. Chernikova, A. et al. Confinement-free annealing induced ferroelectricity in $Hf_{0.5}Zr_{0.5}O_2$ thin films. *Microelectron. Eng* **147**, 15–18 (2015).
31. Mimura, T. et al. Thickness dependence of phase stability in epitaxial $(Hf_xZr_{1-x})O_2$ films. *Phys. Rev. Mater.* **5**, 114407 (2021).
32. Batra, R., Tran, H. D. & Ramprasad, R. Stabilization of metastable phases in hafnia owing to surface energy effects. *Appl. Phys. Lett.* **108**, 172902 (2016).
33. Park, M. H. et al. Understanding the formation of the metastable ferroelectric phase in hafnia-zirconia solid solution thin films. *Nanoscale* **10**, 716–725 (2018).
34. Siannas, N. et al. Metastable ferroelectricity driven by depolarization fields in ultrathin $Hf_{0.5}Zr_{0.5}O_2$. *Commun. Phys.* **5**, 178 (2022).
35. Wang, S. et al. Unconventional ferroelectric-ferroelastic switching mediated by non-polar phase in fluorite oxides. *Adv. Mater.* **37**, 202415131 (2025).
36. Shiraishi, T. et al. Impact of mechanical stress on ferroelectricity in $(Hf_{0.5}Zr_{0.5})O_2$ thin films. *Appl. Phys. Lett.* **108**, 262904 (2016).
37. Batra, R. et al. Factors favoring ferroelectricity in hafnia: a first-principles computational study. *J. Phys. Chem. C* **121**, 4139–4145 (2017).
38. Liu, S. & Hanrahan, B. M. Effects of growth orientations and epitaxial strains on phase stability of HfO_2 thin films. *Phys. Rev. Mater.* **3**, 054404 (2019).
39. Schroeder, U. et al. Impact of different dopants on the switching properties of ferroelectric hafniumoxide. *Jpn J. Appl. Phys.* **53**, 85–89 (2014).
40. Batra, R. et al. Dopants promoting ferroelectricity in hafnia: insights from a comprehensive chemical space exploration. *Chem. Mater.* **29**, 9102–9109 (2017).
41. Zhou, C. et al. Enhanced polarization switching characteristics of HfO_2 ultrathin films via acceptor-donor co-doping. *Nat. Commun.* **15**, 2893 (2024).
42. Glinchuk, M. D. et al. Possible electrochemical origin of ferroelectricity in HfO_2 thin films. *J. Alloys Compd.* **830**, 153628 (2020).
43. Park, M. H. et al. Surface and grain boundary energy as the key enabler of ferroelectricity in nanoscale hafnia-zirconia: a comparison of model and experiment. *Nanoscale* **9**, 9973–9986 (2017).
44. Zhong, H. et al. Large-scale $Hf_{0.5}Zr_{0.5}O_2$ membranes with robust ferroelectricity. *Adv. Mater.* **34**, 2109889 (2022).
45. Li, X. et al. Ferroelastically protected reversible orthorhombic to monoclinic-like phase transition in ZrO_2 nanocrystals. *Nat. Mater.* **23**, 1077–1084 (2024).
46. Alcala, R. et al. The electrode–ferroelectric interface as the primary constraint on endurance and retention in HZO-based ferroelectric capacitors. *Adv. Func. Mater.* **33**, 2303261 (2023).
47. Liu, K. et al. Optimizing the ferroelectric performance of $Hf_{0.5}Zr_{0.5}O_2$ epitaxial film by $La_{0.67}Sr_{0.33}MnO_3$ capping layer. *Adv. Electron. Mater.* **10**, 2400136 (2024).
48. Estandia, S. et al. Domain-matching epitaxy of ferroelectric $Hf_{0.5}Zr_{0.5}O_2$ (111) on $La_{2/3}Sr_{1/3}MnO_3$(001). *Cryst. Growth Des.* **20**, 3801–3806 (2020).
49. Shi, S. et al. Interface-engineered ferroelectricity of epitaxial $Hf_{0.5}Zr_{0.5}O_2$ thin films. *Nat. Commun.* **14**, 1780 (2023).
50. Hojo, H. et al. Atomic structure of a CeO_2 grain boundary: the role of oxygen vacancies. *Nano Lett.* **10**, 4668–4672 (2010).
51. Wang, Z. L. et al. EELS analysis of cation valence states and oxygen vacancies in magnetic oxides. *Micron* **31**, 571–580 (2000).
52. Gong, H. R. et al. Bond strength and electronic structures of coherent Ir/Ir_3Zr interfaces. *Appl. Phys. Lett.* **92**, 211914 (2008).
53. Gong, H. R., He, Y. H. & Huang, B. Y. Bond strength and interface energy between Pd membranes and TiAl supports. *Appl. Phys. Lett.* **93**, 101907 (2008).
54. Rondinelli, J. M., Eidelson, A. S. & Spaldin, N. A. Non-d^0 Mn-driven ferroelectricity in antiferromagnetic $BaMnO_3$. *Phys. Rev. B* **79**, 205119 (2009).
55. Ahn, M. et al. Effects of resonant bonding and structural distortion on the phase change properties of $Sn_2Sb_2Se_5$. *J. Mater. Chem. C* **5**, 7820–7829 (2017).
56. Shportko, K. et al. Resonant bonding in crystalline phase-change materials. *Nat. Mater.* **7**, 653–658 (2008).
57. Zhao, W. et al. Nanoscale grain boundary-weakened Ce–O covalency and surface confinement intrinsically boosting ceria surface oxygen reactivity. *J. Am. Chem. Soc.* **147**, 13050–13058 (2025).
58. Cao, R. et al. Softening of the optical phonon by reduced interatomic bonding strength without depolarization. *Nature* **634**, 1080–1085 (2024).
59. Tian, Z. et al. Phonon conduction in PbSe, PbTe, and $PbTe_{1-x}Se_x$ from first-principles calculations. *Phys. Rev. B* **85**, 184303 (2012).
60. Ai, P. et al. Point-defect-driven flattened polar phonon bands in fluorite ferroelectrics. *npj Comput Mater.* **9**, 119 (2023).
61. Lee, H. J. et al. Scale-free ferroelectricity induced by flat phonon bands in HfO_2. *Science* **369**, 1343–1347 (2020).
62. Estandía, S. et al. Engineering ferroelectric $Hf_{0.5}Zr_{0.5}O_2$ thin films by epitaxial stress. *ACS Appl. Electron. Mater.* **1**, 1449–1457 (2019).
63. Estandia, S. et al. Critical effect of the bottom electrode on the ferroelectricity of epitaxial $Hf_{0.5}Zr_{0.5}O_2$ thin films. *J. Mater. Chem. C* **9**, 3486–3492 (2021).
64. Mueller, S. et al. Ferroelectricity in Gd-doped HfO_2 thin films. *ECS J. Solid State Sci. Technol.* **1**, N123–N126 (2012).
65. Schenk, T. et al. On the origin of the large remanent polarization in La:HfO_2. *Adv. Electron. Mater.* **5**, 1900303 (2019).
66. Banerjee, D. et al. Comprehensive study on the origin of orthorhombic phase stabilization in Gd-doped HfO_2 and DFT calculations. *Phys. Chem. Chem. Phys.* **25**, 21479–21491 (2023).

Methods

Free-standing thin film preparation process

Five-nanometre-thick ZrO_2 thin films, supported by a 30-nm LSMO buffer layer, were epitaxially grown on $SrTiO_3$ (001) substrates using PLD. A XeCl excimer laser, operating at a wavelength of 308 nm with a 4.0 mm² beam spot, was used for the deposition process. The LSMO layer was deposited under a dynamic oxygen pressure of 25 Pa, while the ZrO_2 layer was deposited at a reduced pressure of 13 Pa. Both layers were grown at a temperature of 780 °C, with a laser fluence of 1.25 J cm^{-2} and a repetition rate set to 2 Hz. After deposition, the heterostructures were subjected to an in situ annealing treatment at 650 °C under an oxygen pressure of 10 kPa for a duration of 10 min. Subsequent cooling to room temperature was performed at a controlled rate of 10 °C min^{-1}. The resulting O-phase ZrO_2 thin films are kinetically stabilized through the interplay of surface and GB energies. The films are non-monocrystalline but epitaxial with polymorphic crystalline variants due to different in-plane matching possibilities[35,48]. After growth, the sample was treated with a solution composed of 8 mg potassium iodide (KI), 10 ml hydrochloric acid (HCl) and 100 ml water (H_2O) for approximately 12 h to selectively etch the LSMO buffer layer. The resulting unclamped ZrO_2 thin film was then carefully detached from the substrate by immersing it in deionized water and subsequently retrieved using a transmission electron microscopy copper grid. This sample preparation process minimized the thickness of ZrO_2 thin films, thereby enhancing iDPC–STEM imaging contrast[44].

Electron microscopy characterization

The iDPC–STEM images were recorded at 300 kV using an aberration-corrected (S)TEM (FEI Titan Cubed Themis G2300). To obtain a sufficient signal-to-noise ratio for quantitative analysis, the iDPC image was acquired at 2,048 × 2,048 pixels, with a dwell time of 500 ns and a beam current of 20 pA to avoid beam damage. STEM–EELS spectra were recorded at 200 kV. The probe convergence semi-angle was 20.4 mrad, and the collection semi-angle was in the range of ~50 mrad. We acquired a single 178 pixel × 30 pixel EELS map from a 7.82 nm × 1.32 nm region containing the GB with the Gatan GIF 1069. The dwell time was 0.005 s, and the dispersion was 0.18 eV per channel. The EELS background was fitted and subtracted using the power law.

4D-STEM experiments were performed using a Cs-corrected STEM (JEOL NEOARM200) with an accelerating voltage of 200 kV. The convergence semi-angle was 23 mrad, and the beam current was 20 pA. Each 4D-STEM dataset contained 1,024 × 1,024 convergent beam electron diffraction patterns with a dwell time of 250 µs per pattern. Nuclear charges were assigned as delta functions at each atomic site (47.5 e^- for La/Sr, 25 e^- for Mn and 8 e^- for O) and then convolved with the profile of a 200-kV, 23-mrad probe, which incorporates empirically derived aberrations and a 0.5-Å full width at half maximum Gaussian (to approximate source size), to obtain the nuclear charge density along the GB. The experimental electron charge density profile was subsequently derived by subtracting the nuclear charge density from the total charge density.

Lattice distortion and strain analysis

To obtain quantitative information on the lattice distortion and strain, the positions of the cation atoms were precisely determined by CalAtom software through multiple-ellipse fitting[67]. After that, the area of each quadrilateral, constituted by the four nearest cation atoms, was measured by ImageJ software. The reference value was determined by taking the average of the quadrilaterals within the bulk regions of ZrO_2, which are distant from the GBs. The lattice distortion for each quadrilateral was calculated using

$$\text{lattice distortion} = \frac{S - S_0}{S_0} \times 100\%,$$

where S_0 corresponds to the individual quadrilateral. Subsequently, each quadrilateral represents the reference area, and S is the area of the element, which was assigned a corresponding colour to visually map the lattice distortion, as depicted in Fig. 3d.

The magnitude of lattice strain was defined as the relative deviation of lattice parameters between the strained region and the unstrained bulk reference state corresponding to the pristine O-phase ZrO_2 lattice. To resolve strain anisotropy with respect to GB, we first established a local coordinate system with the GB mirror plane as the reference: the x axis was set parallel to the GB mirror plane, and the y axis was set perpendicular to the GB mirror plane. The strain components ε_x (parallel to GB) and ε_y (perpendicular to GB) were calculated using

$$\varepsilon_x = \frac{a_x - a_0}{a_0} \times 100\%$$

$$\varepsilon_y = \frac{b_y - b_0}{b_0} \times 100\%,$$

where a_0 and b_0 denote direction-resolved statistically averaged in-plane lattice parameters of unstrained bulk ZrO_2, obtained via CalAtom fitting of cation positions in bulk regions away from GBs; a_x and b_y represent the actual in-plane lattice parameters of the target region, including GB-adjacent and bulk areas. Specifically, a_x is the lattice parameter parallel to the GB mirror plane, and b_y is the lattice parameter perpendicular to the GB mirror plane.

Computational details

The DFT calculations were carried out using the projector augmented wave potentials as implemented in VASP[68,69]. The exchange and correlation terms were described by the generalized gradient approximation[70]. A plane-wave cut-off of 500 eV was taken for all calculations. The convergence tolerance of atomic forces was 0.01 eV $Å^{-1}$, and that of total energies was 10^{-6} eV. The k-point sampling number was set large enough that the convergence of the total energies was within 2 meV per atom. Brillouin zone integration was performed using Methfessel–Paxton smearing. Ionic relaxations were allowed in all calculations, with the shape and volume kept fixed. The equilibrium structure for pure ZrO_2 obtained within the convergence criteria is consistent with previous DFT generalized gradient approximation calculations and has been used to construct the supercells. The 1 × 1 × 1 Monkhorst–Pack k-point mesh was used in all calculations of GBs. All GB structures were created using the CrystalMaker software.

Data availability

The data supporting the findings of this study are available within the article and its Supplementary Information. Source data are provided with this paper.

References

67. Zhang, Q. et al. CalAtom: a software for quantitatively analysing atomic columns in a transmission electron microscope image. *Ultramicroscopy* **202**, 114–120 (2019).
68. Kresse, G. & Furthmuller, J. Efficient iterative schemes for ab initio total-energy calculations using a plane-wave basis set. *Phys. Rev. B* **54**, 11169–11186 (1996).
69. Kresse, G. & Hafner, J. Ab initio molecular dynamics for liquid metals. *Phys. Rev. B* **47**, 558–561 (1993).
70. Perdew, J., Burke, K. & Ernzerhof, M. Generalized gradient approximation made simple. *Phys. Rev. Lett.* **77**, 3865–3868 (1996).

Acknowledgements

This work was supported by the National Key R&D Program of China (grant no. 2024YFA1409500 (C.G. and Q.Z.)), the National Natural

Science Foundation of China (grant nos. 52322212 (Q.Z.), 52421001 (L.G.), 52250402 (L.G.), 52025025 (L.G.) and 12222414 (C.G)) and the Youth Innovation Promotion Association of CAS (grant no. Y2022003 (C.G.)).

Author contributions

In this work, Q.Z. and C.G. conceived the project and led conceptualization. S.W., S.S. and A.G. performed data processing and DFT calculations. S.W. and H.Z. carried out the investigation. S.W., A.G. and H.Z. performed visualization. Q.Z., C.G. and L.G. secured funding. Q.Z., L.G. and D.S. managed project administration. K.J., Q.Z., C.G. and L.G. supervised the work. S.W. wrote the original draft; Q.Z., H.Z. and C.G. contributed to review and editing. All authors discussed the results and approved the final manuscript.

Competing interests

The authors declare no competing interests.

Additional information

Extended data is available for this paper at https://doi.org/10.1038/s41563-026-02533-6.

Supplementary information The online version contains supplementary material available at https://doi.org/10.1038/s41563-026-02533-6.

Correspondence and requests for materials should be addressed to Qinghua Zhang, Chen Ge or Lin Gu.

Peer review information *Nature Materials* thanks Florencio Sánchez and the other, anonymous, reviewer(s) for their contribution to the peer review of this work.

Reprints and permissions information is available at www.nature.com/reprints.

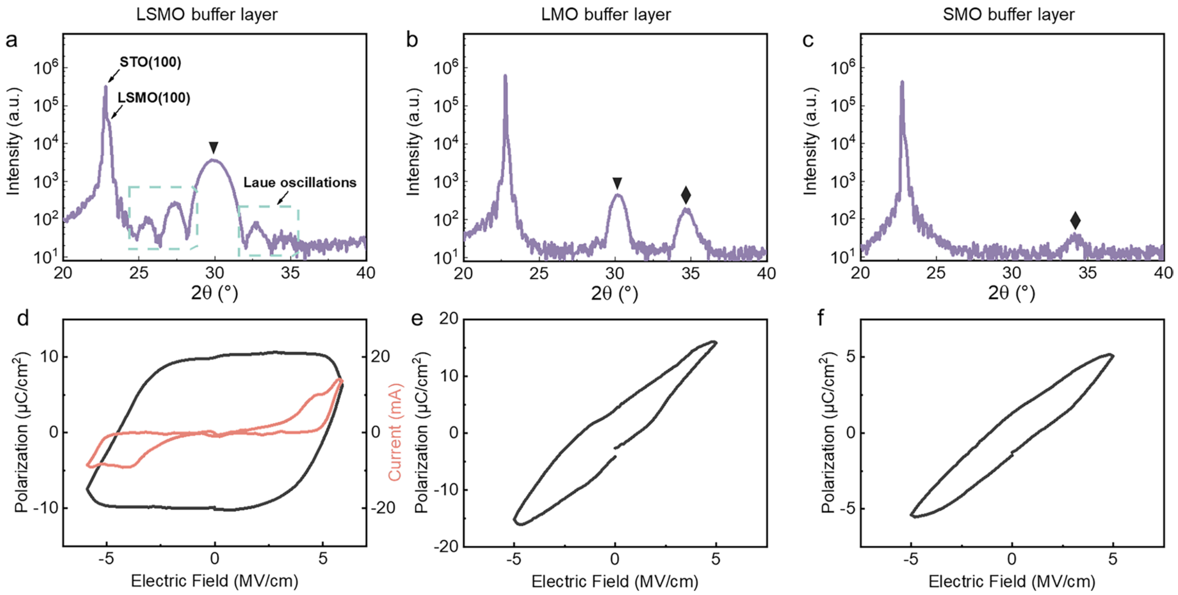

Extended Data Fig. 1 | Macroscopic characteristics of ZrO2 thin films on different buffer layers. (**a**-**c**) XRD patterns of ZrO_2 thin films on LSMO (**a**), LMO (**b**) and SMO (**c**) buffer layers, respectively. Black triangles denote the O-phase (111) plane and black diamonds denote the M-phase (002)/(020) plane. (**d**-**f**) Polarization-electric field (P-E) hysteresis loops of ZrO_2 thin films on LSMO (**d**) with corresponding current-electric field (I-E) loops, LMO (**e**) and SMO (**f**) buffer layers, respectively. For the film grown on LSMO, the positive-up–negative-down (PUND) measurement mode was employed to exclude the leakage current. In contrast, for the films grown on LMO or SMO buffer layers, only simple hysteresis loops were measured due to their extremely weak ferroelectric response. The results clearly demonstrate the crucial role of the LSMO buffer layer in stabilizing the metastable ferroelectric O-phase.

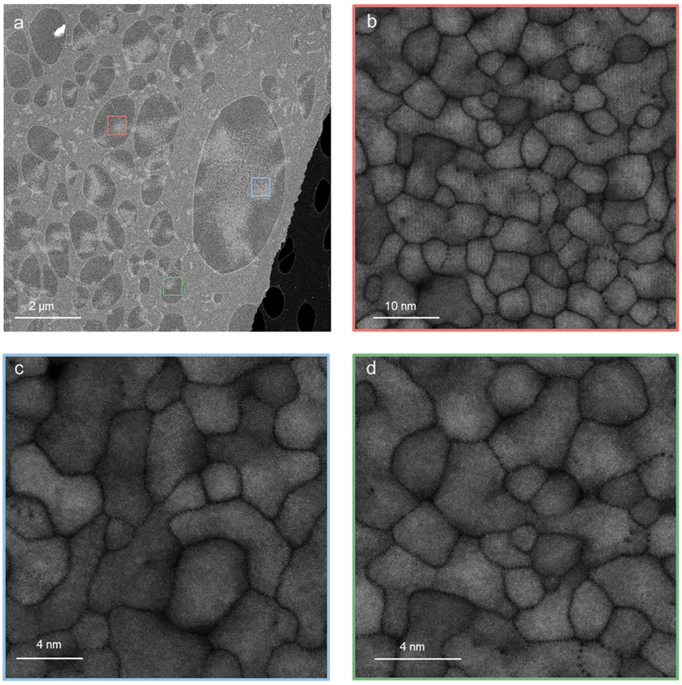

Extended Data Fig. 2 | HAADF images of freestanding ZrO2 thin films at different magnifications. (**a**) Low-magnification overview showing the transferred freestanding films supported on a Cu grid, with bright contrast indicating the thin film regions. The red, blue, and green boxed areas are magnified in (**b-d**), respectively, revealing ordered GBs and a predominant O phase in the ZrO_2 thin films.

https://doi.org/10.1038/s41563-026-02533-6

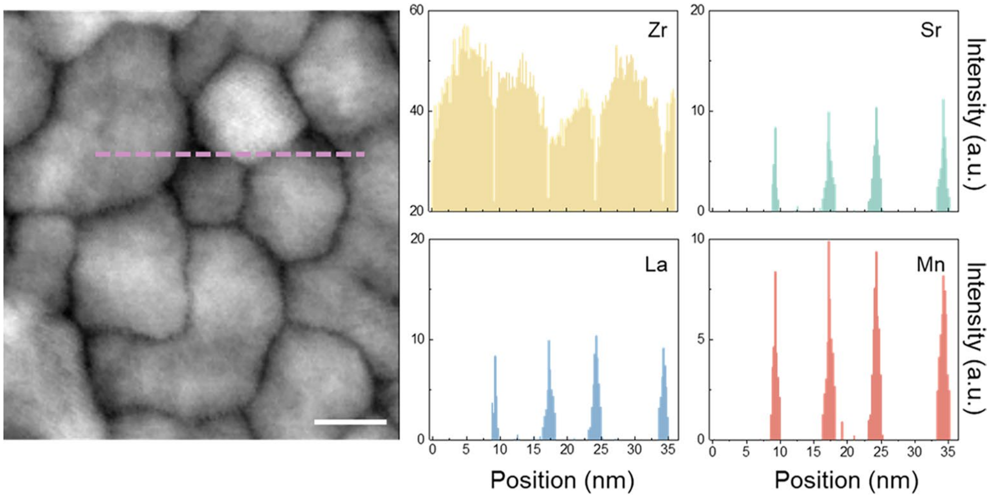

Extended Data Fig. 3 | Line profiles of Zr, La, Sr, and Mn signals obtained along the pink dotted line. The drop in Zr signal corresponds to the peaks of La, Sr, and Mn at GBs. Scale bar: 5 nm.

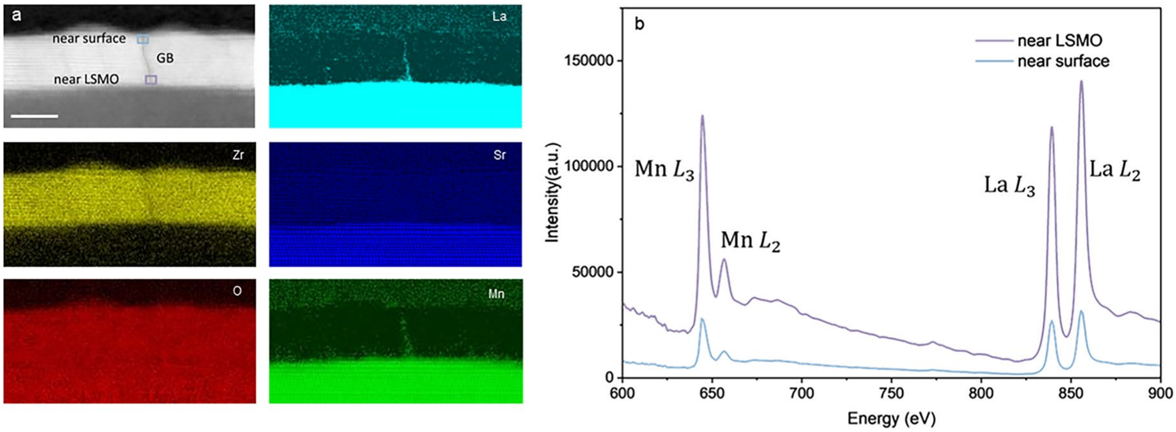

Extended Data Fig. 4 | EELS mappings and corresponding spectra of as-grown ZrO2 thin films on the La0.67Sr0.33MnO3 buffer layer before freestanding. (**a**) EELS mappings: Yellow, red, cyan, blue, and green signals correspond to Zr, O, La, Sr, and Mn elements, respectively. Scale bar: 5 nm. (**b**) EELS spectra: Acquired from two boxed regions within the ZrO_2 thin films. The maps reveal that La, Sr, and Mn from the $La_{0.67}Sr_{0.33}MnO_3$ buffer layer migrate into the ZrO_2 lattice during growth, forming a chemically coupled interface. Meanwhile, a distinct gradient in La and Mn content is present along GBs from the buffer layer to the film top surface, originating from distance-limited diffusion dynamics during deposition. While segregation intensity diminishes near the top surface, the relative stoichiometry and Mn valence state remain nearly unchanged.

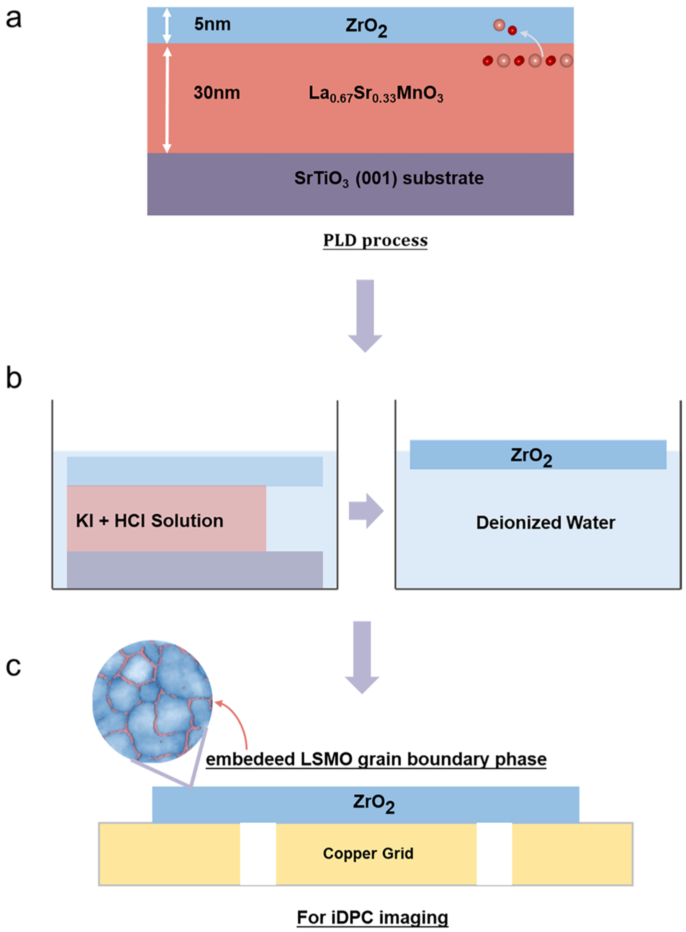

Extended Data Fig. 5 | Schematic of transfer process of ZrO2 films. (**a**) The structure of as-grown samples prepared by PLD. The spheres symbolize the embedded LSMO GB phase formed within the ZrO_2 thin films. (**b**) After PLD, the sacrificial $La_{0.67}Sr_{0.33}MnO_3$ layer is selectively dissolved in an etchant to release the top ZrO_2 film. Then, the unclamped ZrO_2 film is gently removed from the substrate by dipping it in deionized water. (**c**) The released ZrO_2 film is transferred and mounted onto a Cu TEM grid for subsequent plan-view imaging and iDPC-STEM characterization. Given the presence of substantial LSMO GB phases in the pure freestanding ZrO_2 thin films, it can be inferred that these LSMO compounds originate exclusively from the buffer layer used during the initial PLD process.